Acta Pharmaceutica Sinica B 2025;15(10):5431−5443

Chinese Pharmaceutical Association
Institute of Materia Medica, Chinese Academy of Medical Sciences

Acta Pharmaceutica Sinica B

www.elsevier.com/locate/apsb
www.sciencedirect.com

ORIGINAL ARTICLE

Spatiotemporally delivery of Cas9 ribonucleoprotein/DNAzyme logic systems using near-infrared upconversion nanomachine for precise immunotherapy

Chao Chen[a,b,†], Shiyu Du[c,†], Qianglan Lu[c,†], Xueting Shen[a,b], Shuai Ding[a,b], Lihua Qu[d], Yamei Gao[e], Zhiqiang Yin[e,*], Zhe Li[c,*], Yujun Song[c,*], Xin Han[a,b,*]

[a]*The Second Affiliated Hospital of Nanjing University of Chinese Medicine, Nanjing University of Chinese Medicine, Nanjing 210023, China*
[b]*State Key Laboratory on Technologies for Chinese Medicine Pharmaceutical Process Control and Intelligent Manufacture, School of Medicine, Nanjing University of Chinese Medicine, Nanjing 210023, China*
[c]*College of Engineering and Applied Sciences, State Key Laboratory of Analytical Chemistry for Life Science, Nanjing University, Nanjing 210023, China*
[d]*School of Basic Medical Sciences, Xianning Medical College, Hubei University of Science and Technology, Hubei 437000, China*
[e]*Department of Dermatology, the First Affiliated Hospital of Nanjing Medical University, Nanjing 210029, China*

Received 11 February 2025; received in revised form 15 May 2025; accepted 30 May 2025

KEY WORDS

Upconversion nanoparticles;
Cas9 ribonucleoprotein;
Self-assembly DNAzyme;
Gene therapy;
Cancer immunotherapy;
PC linker;

Abstract Gene therapy, harnessing the power of CRISPR-Cas9 and/or DNAzyme systems, stands as a pivotal approach in cancer therapy, enabling the meticulous manipulation of genes pivotal to tumorigenesis and immunity. However, the pursuit of precise gene therapy encounters formidable hurdles. Herein, a near-infrared upconversion theranostic nanomachine is devised and tailors for CRISPR-Cas9/DNAzyme systems mediate precise gene therapy. An ingenious logic DNAzyme system consists of Chain 1 (C1)/Chain 2 (C2) and endogenous lncRNA is designed. We employ manganese modified upconversion nanoparticles for carrying ultraviolet-responsive C1−PC linker−C2 (C_2P) chain and Cas9 ribonucleoprotein (RNP), with outermost coats with hyaluronic acid. Upon reaching tumor microenvironment (TME),

*Corresponding authors.
E-mail addresses: yinzhiqiang@njmu.edu.cn (Zhiqiang Yin), zheli@nju.edu.cn (Zhe Li), ysong@nju.edu.cn (Yujun Song), xhan0220@njucm.edu.cn (Xin Han).
†These authors made equal contributions to this work.
Peer review under the responsibility of Chinese Pharmaceutical Association and Institute of Materia Medica, Chinese Academy of Medical Sciences.

https://doi.org/10.1016/j.apsb.2025.07.010

cGAS−STING signaling; LncRNA

the released Mn^{2+} ions orchestrate a trifecta: facilitating endosomal escape, activating cGAS−STING signaling, and enabling T1-magnetic resonance imaging. Under near-infrared irradiation, Cas9 RNP/C_2P complex dissociates, releasing Cas9 RNP into the nucleus to perform gene editing of Ptpn2, while C1/C2 chains self-assemble with endogenous lncRNA to form a functional DNAzyme system, targeting PD-L1 mRNA for gene silencing. This strategy remodels the TME by activating cGAS−STING signaling and dual immune checkpoints blockade, thus realizing tumor elimination. Our theranostic nanomachine armed with the CRISPR-Cas9/DNAzyme logic systems, represents a resourceful and promising strategy for advancing cancer systemic immunotherapy and precise gene therapy.

1. Introduction

As a promising treatment strategy for malignant tumors, gene therapy focuses on genetic modification to correct or compensate for diseases caused by gene defects and abnormalities, and ultimately achieve therapeutic purposes[1,2]. Functional nucleic acids mediated gene therapy, such as sgRNA-guided CRISPR-Cas9 genome editing system or mRNA cleavage activity of DNAzyme system, which garnered substantial potential for targeting and modifying genes associated with tumorigenesis and immune evasion[3,4]. However, efficient intracellular delivery of functional nucleic acids presents inherent challenges due to their molecular characteristics, especially for CRISPR-Cas9 system must be accurately transfer into the nucleus of targeted cells to achieve its function[5,6]. In contrast to viral vectors, which may evoke concerns over carcinogenesis and immunogenicity, non-viral delivery systems have emerged as highly specific and efficient alternatives, tailored for the delivery of therapeutic functional nucleic acids in disease treatment[7,8]. Despite advancements in delivery systems, gene therapy continues to grapple with issues such as precision targeting, regulation, bioavailability, and long-term safety concerns[9,10], necessitating the urgent exploration of advanced, controllable, and efficient therapeutic functional nucleic acids delivery systems.

On-demand delivery nanosystem based on stimuli-responsive design has been emerged as a promising non-viral vector for gene therapy, which allows for controlled release of genetic payloads through conditioned stimulus mechanism, such as pH value, glutathione, temperature, or photo, ensuring precise gene regulation[11-13]. Among the stimuli-responsive strategies, photo-mediated controllable method has emerged as a promising option for the delivery of functional nucleic acids, with highly spatiotemporal precision[14-17]. Lanthanide doped upconversion nanoparticles (UCNPs), emerging as an innovative nanotransducers, shows the distinguished properties of ultraviolet luminescence, which can be motivated by near-infrared (NIR) light (808 or 980 nm) and conversion of low-energy NIR light into high-energy ultraviolet (UV) light for corresponding biomedical applications[18-20]. Given the superior tissue penetration capabilities of near-infrared (NIR) light, NIR-triggered UCNPs has suitable applications in photoresponsive release of the Cas9 ribonucleoprotein (RNP)[14,21], reaction with the UV-activated photocleavable (PC)-linker[22,23], which makes them an attractive option for spatiotemporal controllable functional nucleic acids delivery system for gene therapy.

Manganese ion has proved to be an effective activator for cGAS−STING signaling, and thus stimulates the innate immune response[24-26]. In this work, we present a spatiotemporal controllable functional nucleic acid delivery system using manganese-modified UCNPs to effectively carry the Cas9 RNP/DNAzyme logic system. This strategy seamlessly integrates gene- and immune-therapy, showing effective tumor repression *in vivo*. Among the Cas9 RNP/DNAzyme logic system, PC linker modified DNA chain was designed as a complementary strand of sgRNA, and connecting Chain 1 (C1) and Chain 2 (C2), which termed as C1−PC linker−C2 (C_2P). The C_2P mixes with the Cas9 RNP to form the Cas9 RNP/C_2P (R/C) complexes that load onto manganese-modified UCNPs (U@M) by electrostatic adsorption, and then encapsulates with CD44-targeting hyaluronic acid (HA)[26,27] to enhance the targeting and stability of nanomachine (termed as U@M-R/C@H) (Fig. 1A). The attachment of HA confers the cellular internalization of the U@M-R/C@H, and the released Mn^{2+} ions assist the endosomal escape[28]. Upon 980 nm NIR light irradiation, the R/C complexes break down and release C1/C2 chains and Cas9 RNP. The Cas9 RNP enters into the nucleus to perform the genome editing behavior, and we employ Ptpn2[29,30], an immune checkpoint gene, as the targeting gene for Cas9 RNP system to reduce immune evasion of tumor. Concurrently, the C1/C2 chains are attracted by endogenous lncRNA *HOTAIR*[31] and self-assemble to form the DNAzyme system for mRNA cleavage with the assistance of Mn^{2+} ions, and the other immune checkpoint gene, *PD-L1* gene is used as the target[24,32]. Moreover, the Mn^{2+} also mediates T1-magnetic resonance imaging and activates the cGAS−STING signaling, thereby amplifying the immune response by triggering type I interferons (IFNs) in the innate immune system and reshaping the tumor immune microenvironment (Fig. 1B and C). Importantly, this near-infrared upconversion triggered theranostic nanomachine simultaneously realizes cGAS−STING signaling activation and dual-immune checkpoint blockade, and exhibits a sustainable antitumor phenotype. Our strategy may have great potential in tumor systemic immunotherapy, precise and controllable gene therapy.

2. Materials and methods

2.1. Ethical statement

This study complies with all relevant ethical regulations. All animal experimental procedures were conducted in accordance with China's Committee for Research and Animal Ethics in compliance with the law for experimental animals and were approved by the Institutional Animal Care and Use Committee of the Nanjing University of Chinese Medicine (approval number: 202210A026).

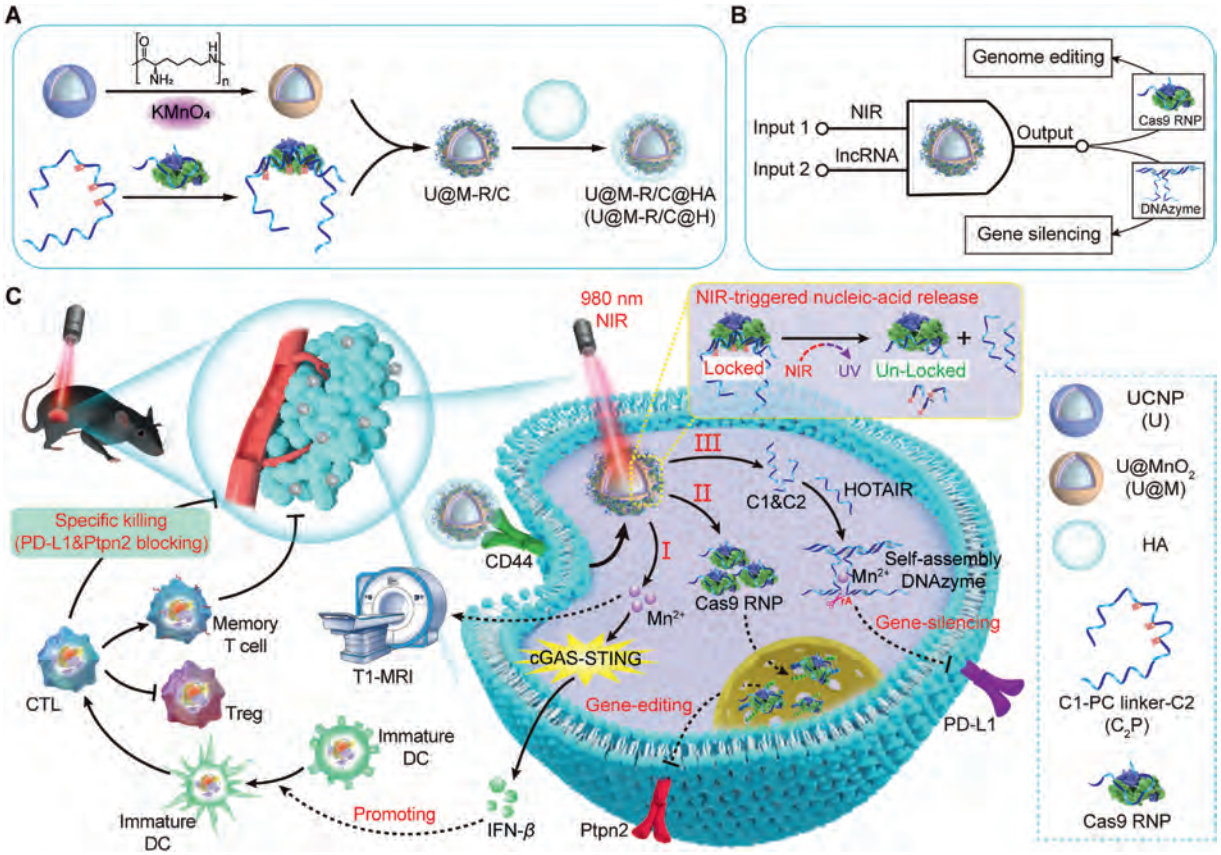

Figure 1 Design of NIR upconversion triggered nanomachine carrying Cas9 RNP/DNAzyme logic systems for precise tumor immunotherapy. (A) Stepwise synthesis of U@M-R/C@H. (B) The Cas9 RNP/DNAzyme logic circuit for precise gene therapy in this work. (C) NIR initiated dual gene regulation nanomachine for precise tumor immunotherapy. Endocytosis of U@M-R/C@H mediated by "HA and CD44 interaction", and releases upconversion nanoparticles (UCNPs) and Cas9 RNP/C_2P (R/C) complexes through MnO_2 layer degrades into Mn^{2+} ions. After exposure to 980 nm NIR light, the R/C complexes is unlocked by ultraviolet (UV) light, which is converted by NIR *via* UCNPs. Subsequently, the released Cas9 RNP targeting Ptpn2 enters into the nucleus to induce genome editing of Ptpn2. Meanwhile, the C1&C2 is self-assembled with endogenous lncRNA HOTAIR to form a "Self-assembly DNAzyme" system, which is catalyzed *via* Mn^{2+} ions to achieve cleavage of *PD-L1* mRNA. Moreover, the Mn^{2+} ions can effectively activate innate immunity by cGAS−STING signaling and simultaneously mediate T1-MRI, thereby realizing the integration of diagnosis and treatment.

2.2. *Reagents and materials*

All reagents used in the experiments were purchased from commercial sources without further purification. $YCl_3 \cdot 6H_2O$, $YbCl_3 \cdot 6H_2O$, $TmCl_3 \cdot 6H_2O$, oleic acid, NH_4F and $KMnO_4$ were purchased from Sigma−Aldrich. The ELISA kit for IFN-β was purchased from Sangon Biotech (Shanghai, China) Co., Ltd., and all oligonucleotides were synthesized and purified by Sangon Biotech (Shanghai, China) Co., Ltd. and the sequences are provided in Supporting Information Tables S1 and S2. Both of FastPure Cell/Tissue Total RNA Isolation Kit, HiScript III RT SuperMix for qPCR (+gDNA wiper), and ChamQ Universal SYBR qPCR Master Mix and T7 Endonuclease I were obtained from Vazyme (Nanjing, China) and Takara (Dalian, China). Cell lysis buffer for Western blotting was purchased from Beyotime (Shanghai, China). ELISA kits for TNF-α, IFN-γ and IL-6 analysis were obtained from Dakewe Bio-engineering Co., Ltd. (Beijing, China). All aqueous solutions were prepared using ultrapure water (18.2 MU, Milli-Q; Millipore). The primary antibodies used in this study were commercially available and listed in Supporting Information Table S3. The morphology and structure evolution of nanoparticles were examined by transmission electron microscopy (TEM, Tecnai G2 F20 X-TWIN, FEI, USA). The cell uptake inhibitor, such as, Methyl-β-cyclodextrin(MβCD), chlorpromazine (CPZ), PolyI, Filipin III were purchased from MedChemExpress (MCE).

2.3. *Preparation of U@M-R/C@H nanomachine*

Upconversion nanoparticles (UCNPs) were first synthesized, that is, 2 mmol/L $LnCl_3$ (Ln = Y, Yb, Tm), 15 mL oleic acid, and 35 mL 1-octachene were mixed and heated to 150 °C for 45 min, then cooled to 50 °C, and methanol containing 8 mmol/L NH_4F and 5 mmol/L NaOH was added. The mixture was heated to 100 °C for 30 min, followed by nitrogen and the reaction temperature was raised to 290 °C, and the heating was stopped after 1.5 h. The mixture was dropped to room temperature and washed three times with ethanol solution to obtain UCNPs. The UCNPs were dispersed in 10 mL of cyclohexane and stirred with 10 mL of 0.1 mol/L hydrochloric acid for 2 h to hydrate. After removing the upper cyclohexane layer, the hydrated UCNPs were collected by centrifugation and washed three times with deionized water. To

modify UCNPs with MnO_2, the hydrated UCNPs were dispersed in 10 mL of 0.1 mmol/L potassium permanganate ($KMnO_4$) solution and stirred vigorously for 4 h, resulting in the deposition of a MnO_2 layer on their surface, forming UCNP@MnO_2. The UCNP@MnO_2 were collected by centrifugation and washed thoroughly with deionized water. Subsequently, 5 mL of UCNP@MnO_2 solution was added to 5 mL of PLL solution (5 mg/mL) under ultrasonication. After stirring for 1 h, the mixture was centrifuged and washed with water to obtain UCNP@MnO_2-PLL. The positively charged PLL coating facilitated the adsorption of Cas9 RNP and C1-PC linker-C2 chains with negative charges to obtain UCNP@MnO_2-R/C nanocomplex. To ensure stability, the UCNP@MnO_2-R/C were further modified by stirring 5 mL of the solution with 5 mL of HA (2 mg/mL) for 1 h to obtain UCNP@MnO_2-R/C@HA nanomachine.

2.4. Mouse tumor model establishment

For the *in situ* tumor mouse model construction, the right flank of C57BL/6 mice was injected subcutaneously with the murine melanoma B16F10 cells (1×10^6 cells). The modeled mice were randomly divided into six groups when the tumor volume of about 80 mm^3, and subsequently treatment of PBS, 980 nm NIR light (L), U@M@H + L, U@M-R/C@H, U@M-R/sC@H + L, U@M-R/C@H + L, respectively. One mg/mL of nanomachine (100 μL) was injected intravenously every other day for 5 consecutive times. For receiving NIR irradiation groups, the mice were exposure to NIR light (1.0 W/cm^2 for 2 min) after 8 h of drug administration. During the treatment process, the body weight and tumor volume were monitored and recorded, and the tumor volume was calculated as Eq. (1):

$$\text{Tumor volume} = 0.5 \times (\text{Length} \times \text{Width}^2) \quad (1)$$

The tumor tissues, peripheral blood, and major organs were collected for further analysis after the mice were sacrificed at the end of experiment.

For the distant metastatic tumor model establishment, six days after B16F10 cells (1×10^6 cells) injected into the right flank of mice as the primary proximal tumor, the modeled mice were randomly divided into six groups and the distant tumor (B16F10 cells, 1×10^5 cells) was transplanted into the left flank of mice. Subsequently, the mice were treated with different formulations every other day for ten days, and the weight of mice and the primary&distant tumor volume was monitored and recorded. The mice were euthanized at the end of experiment, the tumor and spleen tissues of each group were harvested for flow cytometry analysis.

2.5. Flow cytometry analysis

For *in situ* tumor mouse model, the tumor and spleen tissues were performed flow cytometry analysis for the subpopulations of $CD3^+CD4^+$ helper and $CD3^+CD8^+$ cytotoxic T lymphocytes, $CD11c^+CD86^+CD80^+$ dendritic cells (DCs) as well as $CD45^+CD11b^+F4/80^+CD86^+$ M1-like macrophages and $CD45^+CD11b^+F4/80^+CD206^+$ M2-like macrophages. Moreover, for distant metastatic tumor mouse model, the percentage of $CD3^+CD4^+$ helper and $CD3^+CD8^+$ cytotoxic T lymphocytes as well as $CD3^+CD8^+CD44^+CD62L^-$ effector memory T cells (TEMs) in spleens were analyzed.

2.6. Enzyme-linked immunosorbent assay evaluation

The serum was extracted from the peripheral blood by centrifugation and further analyzed by enzyme-linked immunosorbent assay (ELISA). That is, the mice were fasted for 12 h and then peripheral blood was collected through orbital sampling. After standing at room temperature for 4−6 h, the serum was obtained by centrifugation at $1000 \times g$ for 10 min. The levels of serum TNF-α, IFN-γ and IL-6 were determined according to the procedure of ELISA kit.

2.7. Histological analysis

The excised tissues were fixed with paraformaldehyde and embedded in paraffin, and then sectioned into ~4 μm for histological analysis. The major organs and tumor tissues were both performed H&E staining, and the tumor sections were proposed to analysis of immunohistochemistry. Specifically, the tumor sections were stained with murine anti-PD-L1, anti-Ptpn2, anti-Ki-67, or TUNEL, and the histologic analysis was performed at Wuhan Servicebio Biotechnology Co., Ltd. (Wuhan, China). The sections were observed under bright-field microscope (DMi 8, Leica).

2.8. T1-weighted magnetic resonance imaging

For *in vitro* magnetic resonance imaging (MRI) detection, 7.0 T-MRI scanner was used and the T1-MRI properties of U@M-R/C@H (0, 0.1, 0.2, 0.5, 0.8 and 1.0 mmol/L) were detected in pH7.4 and pH6.5 + 10 mmol/L GSH solution. Additionally, for *in vivo* MRI evaluation, PBS or U@M-R/C@H nanomachine were injected intravenously into the modeled mice when the tumor volume of about 100 mm^3. The T1-MRI analysis was performed at 0 and 4 h after drugs administration, and the content of manganese in each group were calculated.

2.9. Statistical analysis

Results are indicated as Mean ± standard deviation (SD). Data were carried out at least three experiments and processed in GraphPad Prism 8 software (GraphPad Software Inc. La Jolla, CA, USA) by two-sided Student's *t*-test and one-way analysis of variance (ANOVA). $^*P < 0.05$, $^{**}P < 0.01$, and $^{***}P < 0.001$ were considered statistical significance, and n.s. means no significance.

3. Results and discussion

3.1. Preparation of near-infrared upconversion triggered nanomachine

A dual-controlled DNAzyme logic system that respond to both exogenous and endogenous triggers was ingeniously designed and fabricated. For the endogenous activation component, the fundamental 8−17 DNAzyme system was dissected into two segments−Chain 1 (C1)/Chain 2 (C2) which recombined to create a lncRNA-activated logical DNAzyme structure (Supporting Information Fig. S1A). For the exogenous-responsive aspect, C1/C2 were interconnected using an ultraviolet (UV) light responsive PC linker. Notably, 980 nm near-infrared (NIR) light was converted into UV light by upconversion nanoparticles (UCNPs) and cleaved the PC linker to liberate the C1/C2 (Fig. S1B). The lanthanide-

doped UCNPs was successfully synthesized and showed a distinct circular morphology under transmission electron microscopy (Supporting Information Fig. S2A). The UCNPs were further modified with Poly-L-lysine (PLL) and $KMnO_4$ to fabricate the UCNP@MnO_2 (U@M) (Fig. S2B). Fluorescence emission spectra result confirmed this transformation, revealing the characteristic $^1I_6 \rightarrow {}^3F_4$ and $^1D_2 \rightarrow {}^3H_6$ transitions from Tm^{3+} ions, and a quenched fluorescence signal from the U@M construct (Fig. S2C). NIR-induced self-assembled DNAzyme was verified using gel electrophoresis. Upon the NIR irradiation, the nucleic acid-UCNP mixtures led to the successful cleavage of C1−PC linker−C2 (C_2P) complex into individual C1 and C2 strands, which spontaneously assembled with HOTAIR to form the HOTAIR−C1−C2 DNAzyme system (Fig. 2A). To validate the catalytic performance of this DNAzyme system, PD-L1 (a classical immune checkpoint gene) substrate was employed, and the gel electrophoresis results confirmed that the lncRNA-driven logic DNAzyme was correctly assembled and realized the effectively cleavage of PD-L1 substrate (Fig. 2B).

Moreover, the C_2P was utilized to lock onto the target sequence of sgRNA and then mixed with the Cas9 nuclease to form the R/C complex, which was electrostatically adsorbed onto U@M and assembled into the U@M-R/C. Further modified with hyaluronic acid (HA) to bolster the stability and targeting efficiency of U@M-R/C, and eventually obtained the U@M-R/C@H nanomachine. The TEM, DLS, and ζ-potential measurements were employed to characterize the synthesis process of U@M-R/C@H. U@M-R/C@H appeared in a regular round state with good dispersity as depicted in TEM images (Fig. 2C), with a hydrodynamic diameter of 171.0 ± 1.06 nm (Supporting Information Fig. S3), and the results of variable potential of UCNPs demonstrated the successful loading of MnO_2 layer, R/C system, and HA modification (Fig. 2E). A mapping representative graph further verified the distribution of these elements (Fig. 2D). The serum stability of U@M-R/C@H was also determined in different times using DLS measurement (Supporting Information Fig. S4A) and TEM observation (Fig. S4B). UCNPs display characteristic absorption peaks in the range of 300−400 nm and 450−500 nm, which are masked by the manganese coating[14]. To test whether the degradation of manganese layer could restore these absorption peaks, varying concentrations of glutathione (GSH) were added to simulate the tumor microenvironment (TME) and facilitated manganese layer degradation. It was showed that the fluorescence spectrum of UCNPs irradiated by a 980 nm laser progressively recovered with increasing GSH concentration, which proved that the addition of manganese coating did not compromise the functionality of UCNPs (Fig. 2F). This conclusion was reinforced by the ultraviolet luminescence reappearance of UCNP under 980 nm NIR light and the color disappearance of the manganese layer (Supporting Information Fig. S5).

With the acidic and GSH-rich conditions prevalent in the TME, the manganese coating degraded to yield Mn^{2+} ions, concurrently releasing the R/C system. The results showed that the Cy5-labeled R/C was discharged and exhibited a pronounced increase of fluorescence intensity in the simulated TME (Supporting Information Fig. S6). The Mn^{2+} ions specific self-assembly DNAzyme system was confirmed by gel electrophoresis results and indicated the effectively cleavage of *PD-L1* mRNA substrate with the aid of Mn^{2+} ions (Fig. 2G). The released Mn^{2+} ions demonstrated augmented imaging properties in T1 magnetic resonance imaging (MRI) (Fig. 2H). The PC linker modified C_2P was cleaved upon NIR irradiation and thus freeing sgRNA along with C1/C2 chains, in which the sgRNA/Cas9 nuclease complexes for gene editing, and the C1/C2 and HOTAIR self-assembled to form the logic DNAzyme system for gene silencing (Supporting Information Fig. S7). Furthermore, an optimization of the R/C loading capacity within U@M was conducted and the results shown that the maximum loading of R/C was achieved when the mass ratio of U@M-PLL to R/C was set at 1:1 (Supporting Information Fig. S8). Thus, all subsequent experimental procedures adhered to this optimal ratio. Overall, these results indicated that U@M-R/C@H was successfully constructed and could slickly self-assembled DNAzyme system for *PD-L1* mRNA cleavage.

3.2. Gene regulation and immunity activation of U@M-R/C@H in vitro

The dual gene therapy system was triggered and released upon internalization of U@M-R/C@H by tumor cells, facilitated by the degradation of manganese layer and irradiation of 980 nm NIR (Fig. 3A). The Confocal Laser Scanning Microscopy (CLSM) was firstly employed to assess the lysosomal escape and nuclear localization of U@M-R/C@H and the results indicated that lysosomal escape began after 4 h of U@M-R/C@H co-incubated with B16F10 cells, followed by significant nuclear co-localization at 8 h, which suggested that U@M-R/C@H possessed the potential to penetrate the nucleus for gene editing purposes (Fig. 3B, Supporting Information Figs. S9 and S10). To investigate the cellular internalization pathway of U@M-R/C@H uptake by B16F10 cells, several typical inhibitors of endocytosis were presented and observed using CLSM, the results indicated that the U@M-R/C@H penetrated the cells through an energy-dependent mechanism involving both clathrin- and caveolin-mediated endocytosis (Supporting Information Fig. S11). To further verify that the HA modification could promote the active targeting ability of the U@M-R/C@H nanomachine, the HA inhibitor and FITC-labeled nanomachine was used and the results suggested that the FITC fluorescence intensity in B16F10 cells treated with HA inhibitor was obviously weaker than that of the un-treated group, indicating that HA modification could significantly increase the cellular endocytosis of nanomachine (Supporting Information Fig. S12). The level of lncRNA HOTAIR was evaluated in the B16F10 cells and found that it was significantly increased compared to the normal skin cells (Supporting Information Fig. S13). Moreover, the cytotoxicity of U@M-R/C@H nanomachine with or without NIR irradiation was evaluated in B16F10 cells (Supporting Information Fig. S14). And then, the gene editing efficiency of NIR-triggered U@M-R/C@H was evaluated by T7 Endonuclease I (T7E1) assay and confirmed the presence of Cas9 RNP cleavage-generated mutants in the PCR fragments and showed that the gene editing efficiency of Ptpn2 gene was 29.8% and 31.1% in the U@M-R/sC@H + Laser (L) and U@M-R/C@H + L groups, respectively, which validating the successful implementation of CRISPR-Cas9 gene editing (Fig. 3C). Importantly, no cleavage by T7EI assay was observed in samples with not subjected to NIR irradiation, which showed excellent controllability of NIR-initiated U@M-R/C@H. The gene editing of Cas9 RNP for Ptpn2 and gene silencing of self-assembly DNAzyme for PD-L1 were verified upon mRNA and protein levels. It was showed that the mRNA and protein levels of Ptpn2 were significant decreased in the U@M-R/sC@H + L and U@M-R/C@H + L treated groups, and the mRNA and protein levels of PD-L1 were obviously reduced only in the U@M-R/C@H + L treated group, which explained as U@M-R/sC@H was

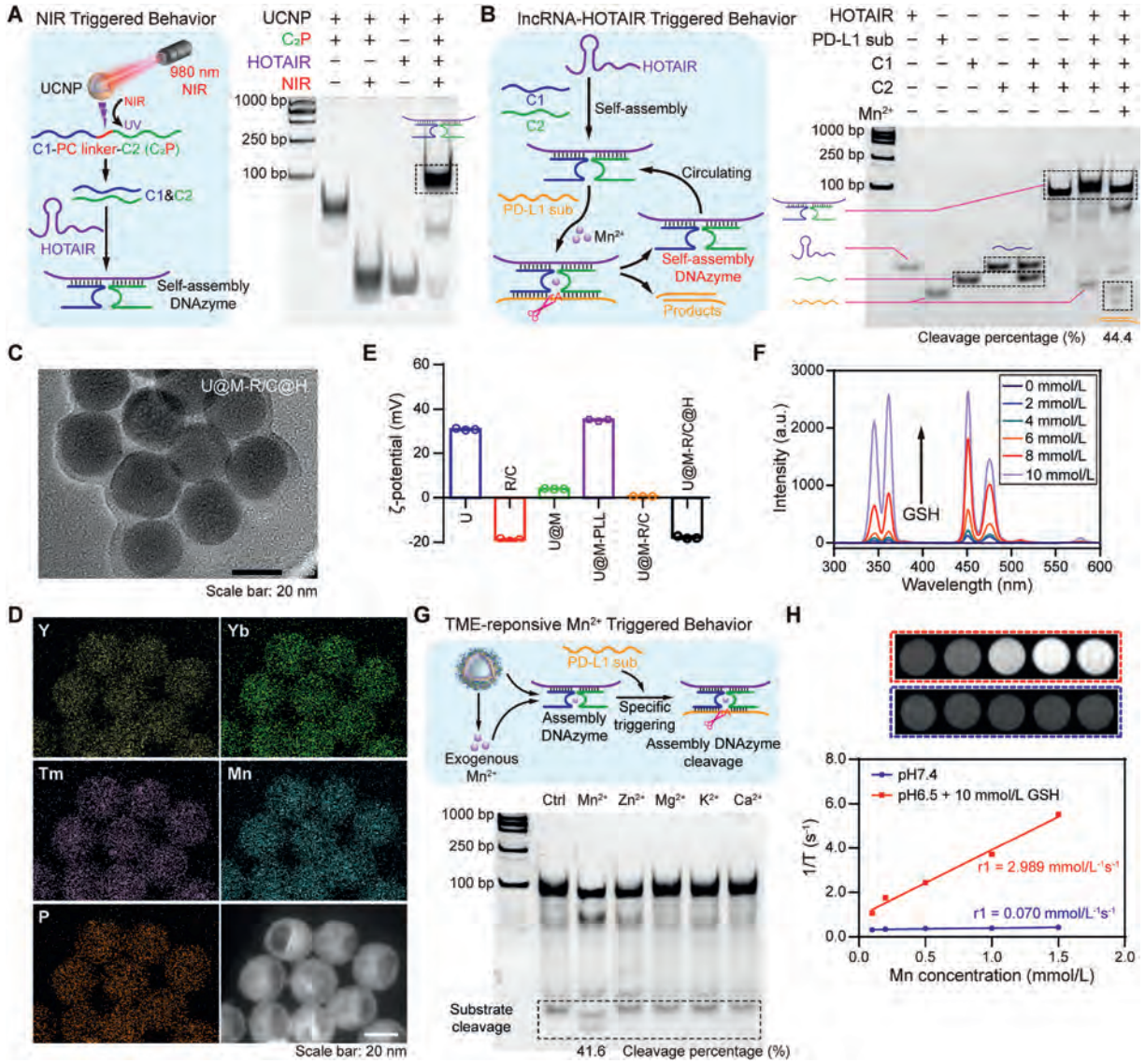

Figure 2 Characterization of NIR upconversion triggered nanomachine. (A) The NIR-triggered behavior of self-assembly DNAzyme system. (B) The lncRNA HOTAIR-initiated behavior of DNAzyme logic system for cleavage of PD-L1 substrate. (C) The representative TEM image of U@M-R/C@H nanomachine. Scale bar = 20 nm. (D) Element mapping of U@M-R/C@H. Scale bar = 20 nm. (E) The ζ-potentials of UCNPs (U), R/C (RNP/C_2P), U@MnO_2 (U@M), U@M-PLL, U@M-R/C, and U@M-R/C@H. (F) Fluorescence spectrum of U@M-R/C@H irradiated by a 980 nm laser after incubation with different concentration of GSH. (G) The Mn^{2+} ions specificity behavior of DNAzyme logic system for PD-L1 substrate cleavage. (H) T1-MR phantom images of U@M-R/C@H under different pH/redox stimuli. Data are expressed as mean ± SD, $n = 3$.

assembled using scrambled C_2P (Fig. 3D and E and Supporting Information Fig. S15). The Mn^{2+} ions have reported that can activate the cGAS−STING signaling and trigger the innate immunity[26]. The crucial IFN-β protein levels were evaluated by the Western blotting and indicated that all Mn^{2+}-based nanomachines could increase the IFN-β expression (Supporting Information Fig. S16). Subsequently, PCR products were analyzed to detect non-homologous end joining repair errors by introducing sticky ends and inserting cloned sequencing into eukaryotic expression vectors, and the results showed a representative list of mutations caused by insertions, base substitutions, or deletions in gene sequencing (Fig. 3F). The gene editing efficiency induced by U@M-R/C@H + L treatment was also evaluated using the high-throughput sequence assay (Supporting Information Fig. S17). Prediction and detection of off-target sites affirmed the precise and conservative nature of Ptpn2 knockout by Cas9 RNP, indicating a low off-target efficiency of the U@M-R/C@H (Fig. 3G).

Considering that the NIR-initiated U@M-R/C@H elicited immune modulation through Mn^{2+} ions stimulation and immune checkpoint blockade, whether U@M-R/C@H could promote maturation of dendritic cells (DCs) *in vitro* was detected. To simulate the concurrent changes in immune cells and tumor cells under identical environmental conditions, bone marrow-derived dendritic cells (BMDCs) and B16F10 cells were co-cultured using a Transwell chamber (Fig. 3H). The co-cultured BMDCs was treated and collected for flow cytometry analysis and the results showed that the percentage of mature DCs ($CD11c^+CD80^+CD86^+$) in treated groups in was notably higher than that of the control group (8.3 ± 2.8%), especially for U@M-R/C@H + L group (26.2 ± 0.9%) (Fig. 3I and Supporting

Information Fig. S18). Furthermore, the supernatant from the lower layer of BMDCs culture system was collected and assayed for TNF-α and IFN-β using ELISA assay, and it was indicated that the TNF-α and IFN-β levels in the supernatant of BMDCs treated with U@M-R/C@H + L was indeed elevated, registering a relative expression level approximately 2.24 times and 13.05 times of the control group, respectively (Fig. 3J and Supporting Information Fig. S19). These results indicated that the NIR-triggered U@M-R/C@H excellent executed the gene regulatory performance and promoted immunity activation *in vitro*.

3.3. *Therapeutic effects of U@M-R/C@H in vivo*

Encouraged by the promising gene editing capabilities and robust immunity of nanomachine in cellular experiments, the *in vivo* antitumor efficiency of U@M-R/C@H was further investigated. The blood compatibility of U@M-R/C@H was firstly assessed and the absence of hemolysis even at a concentration of 500 μg/mL for U@M-R/C@H, indicating the favorable blood compatibility of nanomachine (Supporting Information Fig. S20). Subsequently, the *in vivo* distribution of U@M-R/C@H was

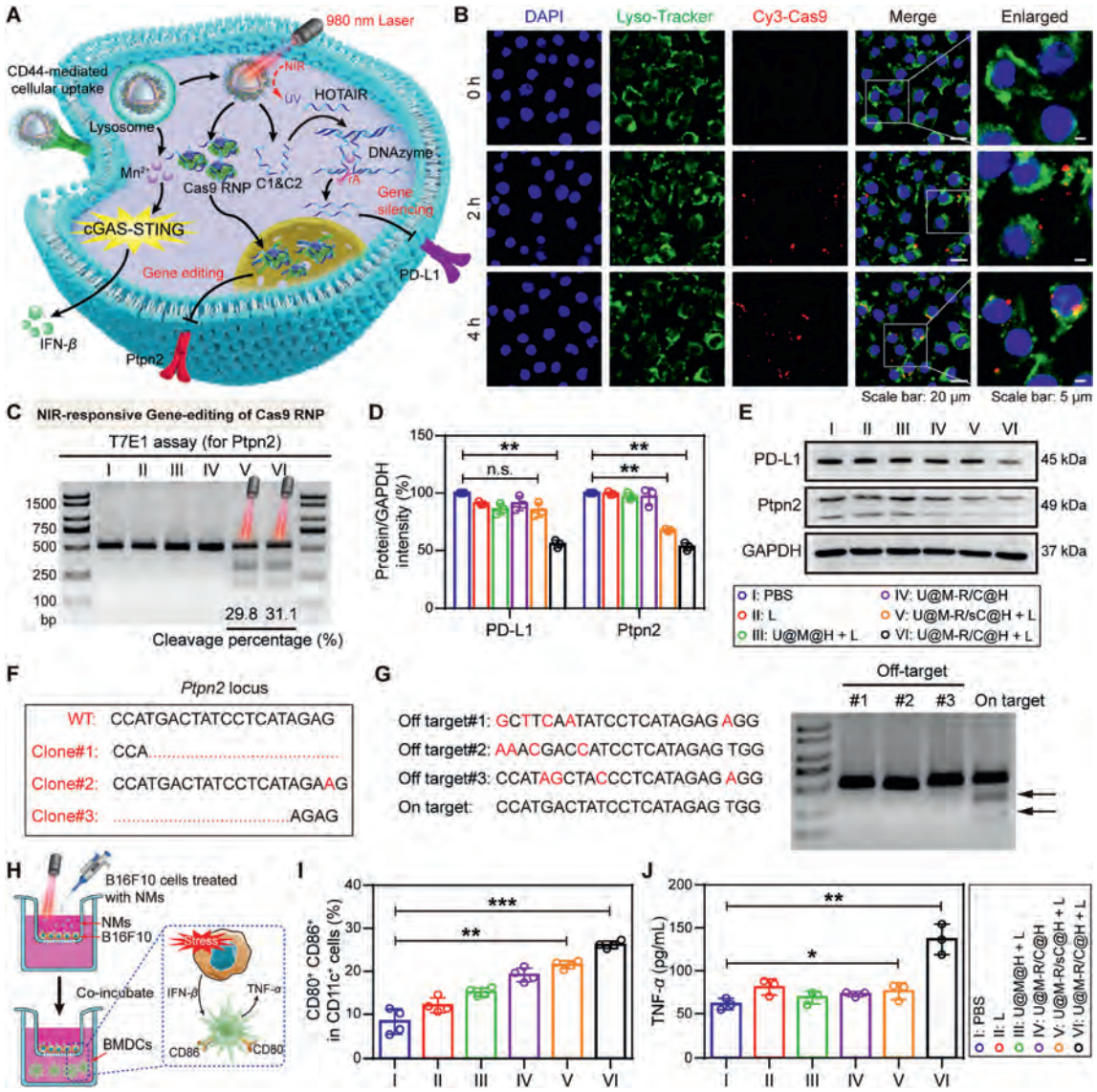

Figure 3 *In vitro* NIR light controllable gene regulation and DCs maturation. (A) Illustration of NIR-initiated *PD-L1* and *Ptpn2* gene regulation, and Mn^{2+} ions mediated cGAS−STING signaling activation. (B) The CLSM images of tumor cells treated with U@M-R/C@H for 0, 2, and 4 h after NIR irradiation (blue, DAPI; green, Lyso-Tracker; red, Cy3). Scale bar = 20 μm; enlarged scale bar = 5 μm. (C) NIR-responsive gene editing behavior of U@M-R/C@H detected by T7E1 assay. (D, E) Western blot and relative quantitative analysis of PD-L1 and Ptpn2 protein levels. (F) PCR product sequencing data of Ptpn2 locus treated with U@M-R/C@H. Representative sequences for indels are shown. (G) Off-target effects were analyzed with U@M-R/C@H treatment using a T7E1 assay. Mismatched bases are shown in red. (H) Schematic illustration of the co-culture transwell assay. (I) Quantitative analysis of $CD80^+CD86^+$ DCs (gated on $CD11c^+$) by flow cytometry. (J) ELISA analysis for the secretion of TNF-α from the supernatant of BMDCs. sC means scrambled C_2P. Data are expressed as mean ± SD, $n = 3$ or 4; $^*P < 0.05$, $^{**}P < 0.01$ and $^{***}P < 0.001$ *vs.* control. n.s., not significant.

evaluated by means of tail vein injection, and Mn-based T1 magnetic resonance imaging was used to locate the U@M-R/C@H. A substantial accumulation of U@M-R/C@H was observed in the tumor site of mice 4 h after injection (Fig. 4A and B). The Mn content in different organs (heart, liver, spleen, lung, kidney, and cancer tissues) was employed as indicator for the biodistribution of U@M-R/C@H and determined using ICP-MS, which suggested the favorable aggregation in tumor region (Supporting Information Fig. S21). Thus, both of the above results affirmed the favorable tumor-targeting capability of U@M-R/C@H. Moreover, the pharmacokinetic analysis of nanomachine *in vivo* was performed, and shown that the elimination half-life of the drug was 83.52 min, the AUC was 629.16 min ng/mL, and the concentration−time curve is presented in Supporting Information Fig. S22.

The B16F10 xenograft bearing mice were randomly divided into five groups when the tumor volume of about 80 mm^3, and treated with different formulations *via* intravenous injection (Fig. 4C). For all groups receiving the 980 nm NIR irradiations, each starting 8 h post-nanomachine administration. The progression of tumor growth and the body weight of mice were meticulously tracked during the entire treatment period. The tumors grew wildly in PBS group, and the U@M-R/C@H + L group indicated

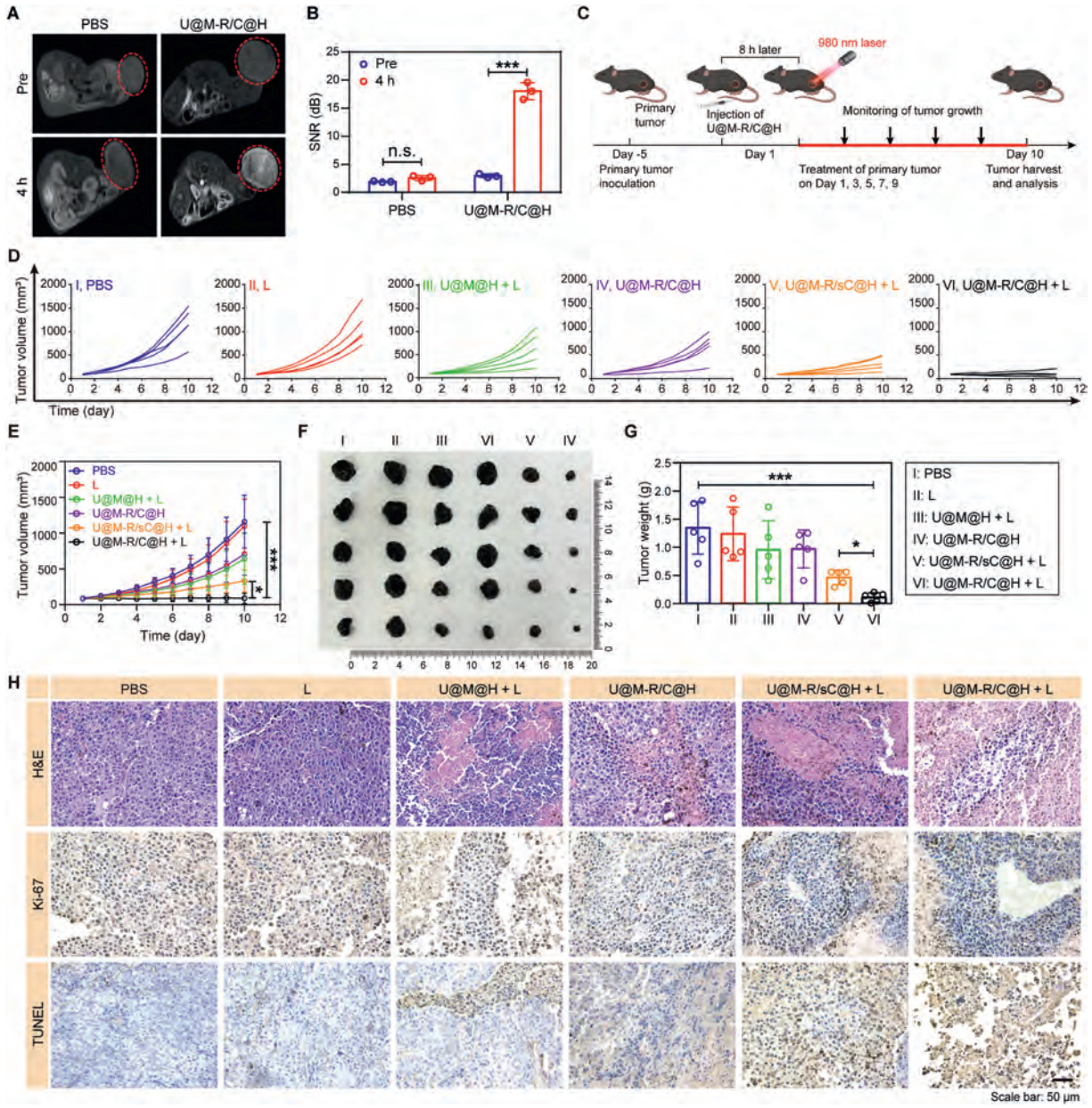

Figure 4 *In vivo* evaluation of U@M-R/C@H for inhibiting primary xenograft. (A) T1 contrast signals after intravenous injection of U@M-R/C@H nanomachine. The red dotted area indicates the tumor region. (B) *In vivo* signal to noise ratio change (SNR) of region analysis for tumor regions. (C) Illustration of the treatment process for primary tumor with nanomachines administration. (D, E) Xenograft growth curves of mice treated with nanomachines. (F) The physical images of harvest tumors. (G) The tumor weights under different formulations. (H) Representative H&E staining and IHC analysis of Ki-67 and TUNEL staining in tumor sections. Scale bar = 50 μm. Data are expressed as mean ± SD, $n = 3$ or 5; $^{*}P < 0.05$ and $^{***}P < 0.001$ *vs.* control. n.s., not significant.

the most robust suppression of tumor growth, which suggested the superior tumor inhibition ability of the nanosystem, and notably, 980 nm NIR illumination alone did not lead to tumor growth inhibition (Fig. 4D and E). The physical images and weights of the isolated tumors were calculated after the euthanasia of mice further confirmed the therapeutic effects of nanomachine (Fig. 4F and G). More precisely, combined treated with the PD-L1 and Ptpn2 checkpoint blockade by the U@M-R/C@H + L resulted in a significantly greater reduction in tumor volume compared to the single blockade of Ptpn2 by U@M-R/sC@H + L. Collectively, these findings confirmed that the U@M-R/C@H effectively suppressed tumor growth when triggered by 980 nm NIR light. In addition, the consistent rise in body weight of mice across all groups implied a negligible level of systemic toxicity of the nanomachine (Supporting Information Fig. S23). Hematoxylin-eosin (H&E) staining of major organs sections indicated no noticeable abnormality or appreciable organ damage (Supporting Information Fig. S24). The standard serum biochemistry assays and complete blood panel tests were also carried out at 1-, 3-, and 7 days post-injection of U@M-R/C@H, the results showed no significant difference in all measured parameters (Supporting Information Fig. S25). All these results indicated low toxicity of U@M-R/C@H *in vivo*.

To authenticate the mechanisms behind tumor suppression, tumor sections of each group were subjected to analysis of H&E and immunohistochemistry (IHC). The results of H&E staining exhibited extensive necrosis in the U@M-R/C@H + L treated group. Meanwhile, *in situ* TUNEL (terminal deoxynucleotidyl transferase-mediated deoxyuridine triphosphate nick end labeling) and Ki-67 staining further confirmed the massive cell apoptosis and most minimum cell proliferation in the U@M-R/C@H + L treatment group (Fig. 4H). Thus, this NIR-initiated nanomachine could accurately accumulate at the tumor site and exerted potent tumor inhibitory effects.

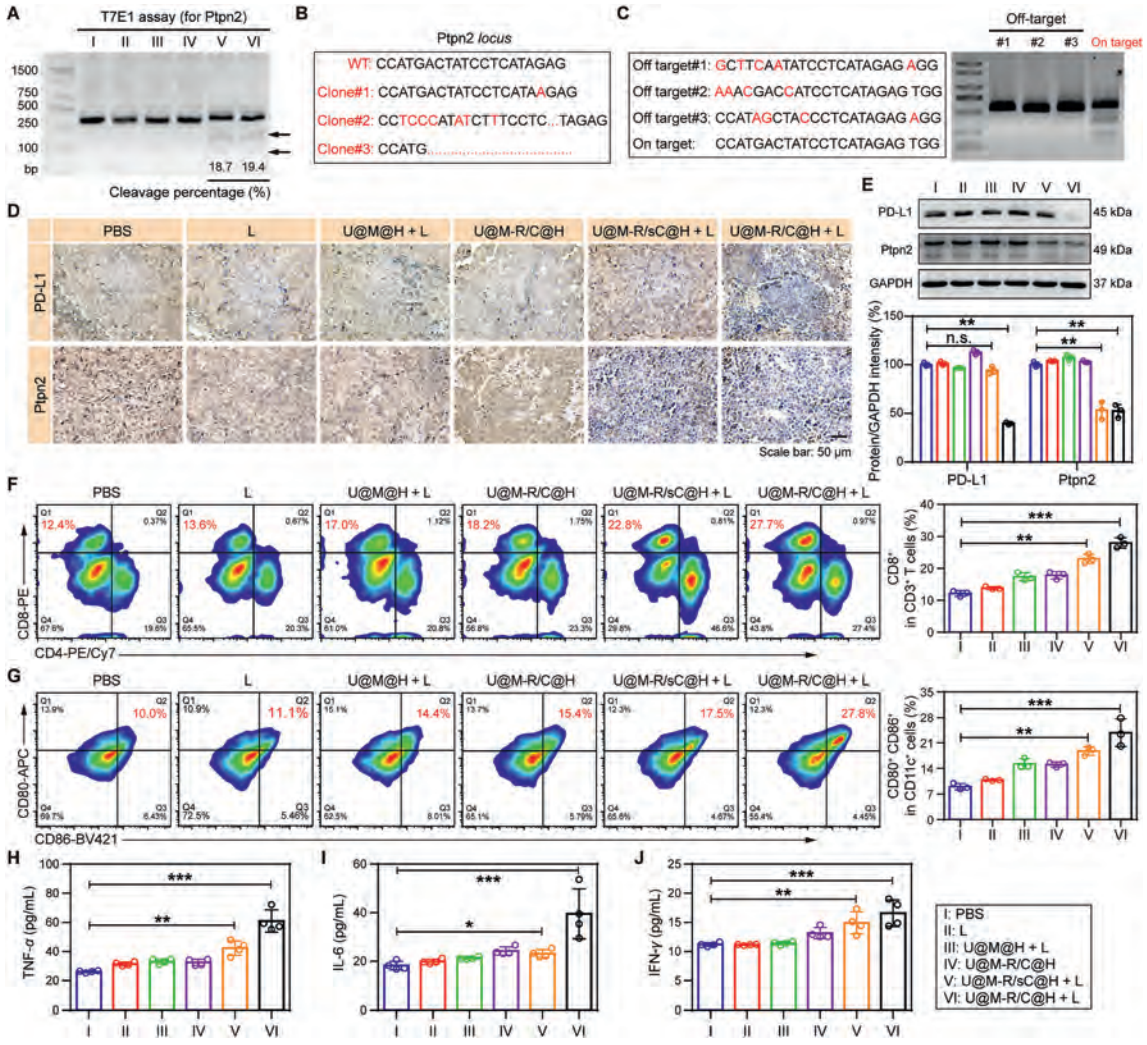

Figure 5 *In vivo* gene regulation and antitumor immune effects of U@M-R/C@H. (A) *In vivo* T7E1 assay for tumor regions with different administrations. (B) Representative sequences for indels of Ptpn2 locus. (C) Off-target effects analysis of tumor tissues. Mismatched bases are shown in red. (D) IHC staining of PD-L1 and Ptpn2 in tumor sections. Scale bar = 50 μm. (E) Western blot analysis of PD-L1 and Ptpn2 protein levels in tumor tissues. (F) Representative flow cytometry plots and quantitative analysis of $CD4^+$ and $CD8^+$ T cells (gated on $CD3^+$ T cells) in spleen. (G) Flow cytometry analysis of matured DCs ($CD80^+CD86^+$ gated on $CD11c^+$ cells) in tumors. Expression levels analysis of (H) TNF-α, (I) IL-6, and (J) IFN-γ in serum by ELISA assay. Data are expressed as mean ± SD, $n = 3$ or 4; $^*P < 0.01$, $^{**}P < 0.01$ and $^{***}P < 0.001$ *vs.* control.

3.4. *Robust gene regulation and antitumor immunity of U@M-R/C@H in vivo*

The gene editing efficiency of Ptpn2 in tumor sections treatment of U@M-R/C@H were detected using T7EI assay, and the apparent frequency of mutations were observed in the U@M-R/sC@H + L (18.7%) and U@M-R/C@H + L (19.4%) treated groups, respectively (Fig. 5A). The predicted list of mutations (insertions or base substitutions) in tumor tissues with treatment of U@M-R/C@H + L was performed (Fig. 5B), and the off-target activities in tumor tissues was also evaluated and identified the low off-target efficiency of U@M-R/C@H *in vivo* (Fig. 5C). In addition, the gene regulation efficiency of NIR-triggered nanomachine were confirmed using IHC staining and Western blotting of PD-L1 and Ptpn2. The lowest PD-L1 expression was observed in tumor sections treated with U@M-R/C@H + L, demonstrating the *in vivo* gene silencing effect of DNAzyme from the nanomachine. The expression levels of Ptpn2 in the U@M-R/sC@H + L and U@M-R/C@H + L groups were lower than those in the other groups, indicating the *in vivo* gene editing efficacy of Cas9 RNP from the nanomachine (Fig. 5D). The results of Western blot analysis were consistent with the trend of IHC staining for PD-L1 and Ptpn2 (Fig. 5E), and both indicated the potent gene regulation ability of NIR-triggered U@M-R/C@H *in vivo*. The cGAS−STING signaling activation was also confirmed in the tumor tissues using Western blotting and showed that the upregulated IFN-β, p-STING, and pTBK1 protein levels were observed in the both Mn^{2+}-based nanomachines treatment groups (Supporting Information Fig. S26).

In the application strategy of this NIR-initiated nanomachine for tumor inhibition, the robust antitumor immunity will be induced after gene regulation and cGAS−STING signaling activation. As the DCs and infiltrated cytotoxic T lymphocytes (CTLs) play a crucial role in initiating innate and adaptive immunities, the percentage of CTLs and matured DCs in tumors and spleens is mainly evaluated through flow cytometry. The

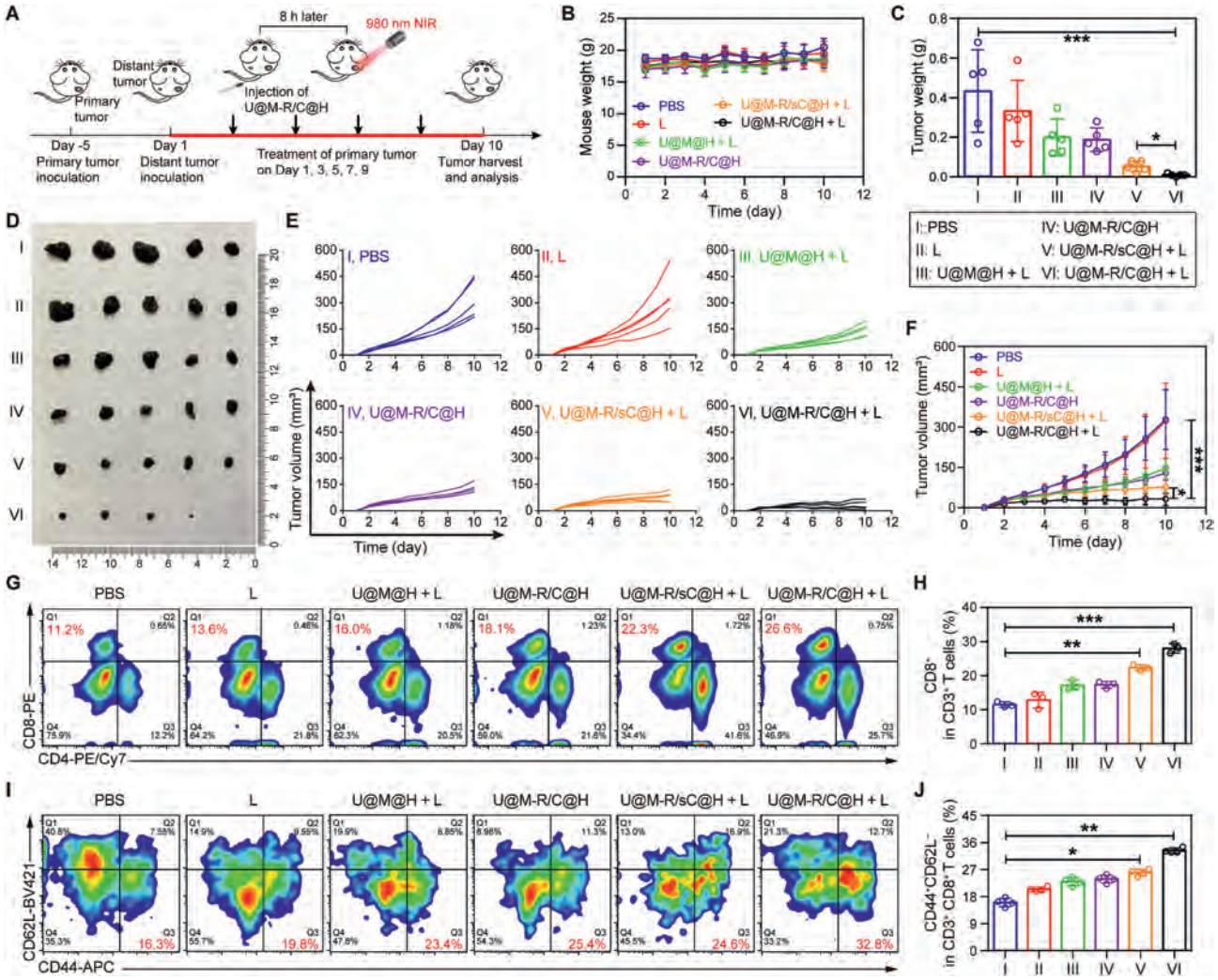

Figure 6 *In vivo* evaluation of U@M-R/C@H mediated long-term antitumor immunity. (A) Illustration of *in vivo* experimental design for nanomachines against both primary and distal xenografts. (B) The mouse weights changes of different treatment groups. (C) The tumor weight of excised distal tumors. (D) The corresponding digital images of excised distal xenografts. (E, F) The growth curve of distal tumors treated with nanomachines. (G, H) Representative flow cytometry plots and quantitative analysis of $CD4^+$ and $CD8^+$ T cells (gated on $CD3^+$ T cells) in spleens. (I) Flow cytometric analysis images of TEMs ($CD3^+CD8^+CD44^+CD62L^-$) in spleens. Data are expressed mean ± SD, $n = 3$ or 5; $^*P < 0.05$, $^{**}P < 0.01$ and $^{***}P < 0.001$ *vs.* control.

percentage of CTLs ($CD3^+CD4^-CD8^+$) were identified in the spleens, and the $CD8^+$ T cells population of U@M-R/C@H + L group (27.9 ± 1.6%) and U@M-R/sC@H + L group (23.0 ± 1.4%) were higher than those in the PBS treated group (12.1 ± 0.9%) (Fig. 5F). For the percentage of matured DCs population ($CD11c^+CD80^+CD86^+$), the U@M-R/C@H + L group (23.8 ± 3.8%) and U@M-R/sC@H + L group (18.8 ± 1.1%) showed a stronger ability to promote DCs maturation than the U@M-R/C@H (15.1 ± 0.7%), U@M@H + L (15.3 ± 1.4%), L (10.8 ± 0.25%), and control group (9.0 ± 0.9%) (Fig. 5G). It was noteworthy that only irradiation of 980 nm laser did not induce DCs maturation and promoted $CD8^+$ T cells population, and the immunity induction of U@M-R/C@H and U@M@H + L could be interpreted as cGAS−STING signaling activation by Mn^{2+} ions. The quantity of M1-like ($CD11b^+F4/80^+CD86^+$) and M2-like ($CD11b^+F4/80^+CD206^+$) macrophages in tumors were also determined by flow cytometry, and the results indicated that the U@M-R/C@H + L treatment (M1, 39.9 ± 1.3%, M2, 20.9 ± 0.8%) obvious promoted the transformation from tumor-associated M2 to M1, compared with the control group (M1, 28.5 ± 0.4%, M2, 29.4 ± 0.9%), which demonstrating the immune checkpoint blockade and cGAS−STING signaling activation achieved remodeling of TME (Supporting Information Fig. S27). To further confirm the antitumor immunity of NIR-triggered nanomachine, the levels of tumor necrosis factor-α (TNF-α), interleukin-6 (IL-6), and interferon-gamma (IFN-γ) released by immune cells were evaluated. The serum cytokine levels of TNF-α, IL-6, and IFN-γ in the U@M-R/C@H + L treatment group were higher than those in the other groups (Fig. 5H−J), which further amplified the antitumor immunity. These evidences suggested that the NIR-triggered nanomachine effectively stimulated both DCs and CTLs, thereby triggering a heightened state of immune activation.

3.5. Long-term antitumor immunoactivities effects of U@M-R/C@H in vivo

An ideal tumor therapeutic strategy should ideally eliminate the local tumor while concurrently stimulate a systemic immune response and inhibit cancer cell metastasis. To further confirm the systemic impacts of NIR-initiated nanomachine, a dual tumor model was established by orthotopic injection of B16F10 cells into both the right and left flank of mice as primary and distant tumors, respectively. After free growth of the primary tumor for six-days, the second xenograft was inoculated on the opposite side of mice, and a succession of five synchronized treatments (intravenously injection of nanosystem and subsequently irradiation of 980 nm NIR) were performed (Fig. 6A). The changes in body weight of mice as well as the volumes of both primary and distant tumors were diligently monitored and recorded. Obviously, no significant changes in the body weight of mice treated with the NIR-initiated nanomachine (Fig. 6B). For primary tumors, the changes in physical images of xenograft, tumor weight and tumor growth curve of each group were consistent with the previous results of single-tumor animal model of mice (Supporting Information Fig. S28). Importantly for distant tumors model, the tumor physical image and weight analysis indicated that the U@M-R/C@H + L group significantly decreased the weight of xenograft compared with the other groups, including the U@M-R/sC@H + L group (Fig. 6C and D). Recording results of the distant tumor growth curve showed that the progression of tumor growth with treatment of U@M-R/C@H + L (30.4 ± 22.9 mm^3) was obviously inhibited, compared with the U@M-R/sC@H + L (76.6 ± 30.8 mm^3) and PBS (327.6 ± 111.2 mm^3) treated groups (Fig. 6E and F).

To further investigate the inhibitory effect of distant tumor was caused by the systemic immune effects of U@M-R/C@H with 980 nm NIR irradiation, the cell population analysis of $CD8^+$ CTLs and effector memory T cells (TEMs) was performed using flow cytometry. It was found that U@M-R/C@H + L (28.0 ± 1.4%) significantly increased the cell percentage of CTLs compared with the U@M-R/sC@H + L (22.3 ± 0.8%) and PBS (11.5 ± 0.8%) groups (Fig. 6G and H). Moreover, the cell population analysis of TEMs ($CD3^+CD8^+CD44^+CD62L^-$) in spleen showed that a notable upregulation of TEMs was observed in U@M-R/C@H + L (33.3 ± 0.9%) treated group than that in the U@M-R/sC@H + L (26.0 ± 1.1%) and PBS (16.1 ± 1.4%) groups (Fig. 6I and J). The augmented infiltration of CTLs and TEMs offered robust support for the enduring anti-tumor immunological benefits afforded by the U@M-R/C@H with NIR irradiation therapeutic approach, underscoring its potential to evoke a durable systemic immune response against cancer.

4. Conclusions

CRISPR-Cas9 or DNAzyme systems mediated gene therapy tools have a promising potential for disease treatment, including tumor. Up to now, multiple studies have combined CRISPR-Cas9 and DNAzyme systems for the treatment of tumors. For example, Tang et al.[33] constructed a Trojan horse-like DNAzyme functionalized nanocapsule for miRNA responsive CRISPR/Cas9 delivery and tumor therapy. Additionally, Li et al.[34] reported a proton-activatable DNA-based nanosystem with co-delivery of CRISPR-Cas9 and DNAzyme for combined gene therapy in breast cancer. Unlike to the above investigation of the existing DNAzyme system, the nanomachines assembled in this study employed an innovative NIR responsive method, and the locked chain C_2P (UV-photocleavage chain) used for blocking the targeted sequence of sgRNA, and then self-assembly formed a DNAzyme system under NIR irradiation. Moreover, PD-L1 blockade mainly dissolves the "brake" signal of T cells, while Ptpn2 inhibition enhances the “throttle” signal of T cells, the dual-gene editing of PD-L1 and Ptpn2 properly solves the problem of drug resistance caused by single inhibition. The Mn^{2+} modification plays a dual role: i) for catalyzing DNAzyme system to mRNA cleavage; ii) for activating the systemic innate immune system and combined dual immune checkpoint blockade therapy (PD-L1 and Ptpn2 blocked).

In summary, a NIR upconversion triggered and TME-responsive theranostic nanomachine carrying Cas9 RNP/DNAzyme logic systems was successfully constructed and tailored for T1-MRI and precise tumor immunotherapy through in combination with gene editing of Cas9 RNP, gene silencing of DNAzyme, and cGAS−STING signaling activation. The C1 and C2 strands were engineered to self-assemble with the endogenous lncRNA, thereby assembling a functional DNAzyme system. A PC linker was ingeniously linked the C1 and C2, and complementary base pairing was performed with sgRNA, and then mixed with the Cas9 nuclease. The nanomachine was synthesized based on the manganese coated UCNPs carrying the R/C complex and outer modification of HA. This nanomachine has been exhibited the inhibitory effects of both primary and distant tumor through activating the systemic immune responses. The potential mechanisms of systemic anti-tumor immunity can be explained as

follows: i) The degradation of manganese layer within TME facilitates the lysosome escape and activates the cGAS−STING signaling. ii) Combined blockade of two immune checkpoint genes, *i.e*., Cas9 RNP gene editing of Ptpn2 and self-assembly DNAzyme gene silencing of PD-L1. Thus, this nanomachine can be effectively synergistic combined in a NIR light controllable manner to promote DCs maturation, CTLs infiltration, macrophages polarization and TEMs proliferation, which results in systemic immunity to eliminate tumors.

Acknowledgments

This work was supported by the National Natural Science Foundation of China (82302365 and 32471475); Supporting project of Nanjing University of Chinese Medicine to NSFC (XPT82302365, China); Yangtze River Delta Joint Sci-tech Innovation and Research Projects (2023CSJZN0600, China); the Innovation Projects of State Key Laboratory on Technologies for Chinese Medicine Pharmaceutical Process Control and Intelligent Manufacture (NZYSKL240201, China); Jiangsu Key Discipline Construction Fund of the 14th Five-Year Plan (Biology); Natural Science Foundation of Hubei Province (No. 2024AFB517, China); Natural Science Foundation of the Higher Education Institutions of Jiangsu Province (23KJB310015, China).

Author contributions

Chao Chen, Shiyu Du and Qianglan Lu performed characterization of materials. Chao Chen, Shiyu Du, Xueting Shen, Lihua Qu, Yamei Gao and Shuai Ding assisted in cell experiments and analysis. Chao Chen, Qianglan Lu and Shiyu Du performed the *in vivo* evaluation. Chao Chen and Xin Han wrote the manuscript with feedback from all the authors. Zhiqiang Yin, Zhe Li, Yujun Song and Xin Han conceived the idea, designed the experiments, and supervised the project.

Conflicts of interest

The authors declare no conflicts of interest.

Appendix A. Supporting information

Supporting information to this article can be found online at https://doi.org/10.1016/j.apsb.2025.07.010.

References

1. High KA, Roncarolo MG. Gene therapy. *N Engl J Med* 2019;**381**:455−64.
2. Brody H. Gene therapy. *Nature* 2018;**564**:S5.
3. Chancellor D, Barrett D, Nguyen-Jatkoe L, Millington S, Eckhardt F. The state of cell and gene therapy in 2023. *Mol Ther* 2023;**31**:3376−88.
4. Li T, Yang Y, Qi H, Cui W, Zhang L, Fu X, et al. CRISPR/Cas9 therapeutics: progress and prospects. *Signal Transduct Targeted Ther* 2023;**8**:36.
5. Micura R, Hobartner C. Fundamental studies of functional nucleic acids: aptamers, riboswitches, ribozymes and DNAzymes. *Chem Soc Rev* 2020;**49**:7331−53.
6. Chen C, Zhong W, Du S, Li Y, Zeng Y, Liu K, et al. Intelligent nanotherapeutic strategies for the delivery of CRISPR system. *Acta Pharm Sin B* 2023;**13**:2510−43.
7. Song X, Liu C, Wang N, Huang H, He S, Gong C, et al. Delivery of CRISPR/Cas systems for cancer gene therapy and immunotherapy. *Adv Drug Deliv Rev* 2021;**168**:158−80.
8. Xie S, Sun W, Fu T, Liu X, Chen P, Qiu L, et al. Aptamer-based targeted delivery of functional nucleic acids. *J Am Chem Soc* 2023;**145**:7677−91.
9. Rogers ML, Rush RA. Non-viral gene therapy for neurological diseases, with an emphasis on targeted gene delivery. *J Control Release* 2012;**157**:183−9.
10. Kargaard A, Sluijter JPG, Klumperman B. Polymeric siRNA gene delivery-transfection efficiency *versus* cytotoxicity. *J Control Release* 2019;**316**:263−91.
11. Deng W, Chen W, Clement S, Guller A, Zhao Z, Engel A, et al. Controlled gene and drug release from a liposomal delivery platform triggered by X-ray radiation. *Nat Commun* 2018;**9**:2713.
12. Yang P, Zhu F, Zhang Z, Cheng Y, Wang Z, Li Y. Stimuli-responsive polydopamine-based smart materials. *Chem Soc Rev* 2021;**50**:8319−43.
13. Zhuo C, Zhang J, Lee JH, Jiao J, Cheng D, Liu L, et al. Spatiotemporal control of CRISPR/Cas9 gene editing. *Signal Transduct Targeted Ther* 2021;**6**:238.
14. Pan Y, Yang J, Luan X, Liu X, Li X, Yang J, et al. Near-infrared upconversion-activated CRISPR-Cas9 system: a remote-controlled gene editing platform. *Sci Adv* 2019;**5**:eaav7199.
15. Chen C, Ma Y, Du S, Wu Y, Shen P, Yan T, et al. Controlled CRISPR-Cas9 ribonucleoprotein delivery for sensitized photothermal therapy. *Small* 2021;**17**:e2101155.
16. Cai W, Luo T, Mao L, Wang M. Spatiotemporal delivery of CRISPR/Cas9 genome editing machinery using stimuli-responsive vehicles. *Angew Chem Int Ed Engl* 2021;**60**:8596−606.
17. Yi K, Kong H, Lao YH, Li D, Mintz RL, Fang T, et al. Engineered nanomaterials to potentiate CRISPR/Cas9 gene editing for cancer therapy. *Adv Mater* 2024;**36**:e2300665.
18. Chen G, Ma B, Xie R, Wang Y, Dou K, Gong S. NIR-induced spatiotemporally controlled gene silencing by upconversion nanoparticle-based siRNA nanocarrier. *J Control Release* 2018;**282**:148−55.
19. Ovais M, Mukherjee S, Pramanik A, Das D, Mukherjee A, Raza A, et al. Designing stimuli-responsive upconversion nanoparticles that exploit the tumor microenvironment. *Adv Mater* 2020;**32**:e2000055.
20. Hlavacek A, Farka Z, Mickert MJ, Kostiv U, Brandmeier JC, Horak D, et al. Bioconjugates of photon-upconversion nanoparticles for cancer biomarker detection and imaging. *Nat Protoc* 2022;**17**:1028−72.
21. Song N, Fan X, Guo X, Tang J, Li H, Tao R, et al. A DNA/upconversion nanoparticle complex enables controlled co-delivery of CRISPR-Cas9 and photodynamic agents for synergistic cancer therapy. *Adv Mater* 2024;**36**:e2309534.
22. Yu F, Li X, Zhao J, Zhao Y, Li L. Photoactivated DNA assembly and disassembly for on-demand activation and termination of cGAS−STING signaling. *Angew Chem Int Ed Engl* 2023;**62**:e202305837.
23. Zhang J, Zhao P, Li W, Ye L, Li L, Li Z, et al. Near-infrared light-activatable spherical nucleic acids for conditional control of protein activity. *Angew Chem Int Ed Engl* 2022;**61**:e202117562.
24. Chen C, Du SY, Lu QL, Liu KG, Pan YC, Jiang YQ, et al. Tumor-associated miRNAs activated HCR-DNAzyme theranostic nanosystem to trigger innate- and adaptive-immune responses for long-term immunotherapy. *Chem Eng J* 2023;**473**:145192.
25. Lv M, Chen M, Zhang R, Zhang W, Wang C, Zhang Y, et al. Manganese is critical for antitumor immune responses *via* cGAS−STING and improves the efficacy of clinical immunotherapy. *Cell Res* 2020;**30**:966−79.
26. Wang C, Guan Y, Lv M, Zhang R, Guo Z, Wei X, et al. Manganese increases the sensitivity of the cGAS−STING pathway for double-stranded DNA and is required for the host defense against DNA viruses. *Immunity* 2018;**48**:675−687 e7.

27. Bhattacharyya M, Jariyal H, Srivastava A. Hyaluronic acid: more than a carrier, having an overpowering extracellular and intracellular impact on cancer. *Carbohydr Polym* 2023;**317**:121081.
28. Fan N, Chen K, Zhu R, Zhang Z, Huang H, Qin S, et al. Manganese-coordinated mRNA vaccines with enhanced mRNA expression and immunogenicity induce robust immune responses against SARS-CoV-2 variants. *Sci Adv* 2022;**8**:eabq3500.
29. Manguso RT, Pope HW, Zimmer MD, Brown FD, Yates KB, Miller BC, et al. *In vivo* CRISPR screening identifies Ptpn2 as a cancer immunotherapy target. *Nature* 2017;**547**:413−8.
30. Baumgartner CK, Ebrahimi-Nik H, Iracheta-Vellve A, Hamel KM, Olander KE, Davis TGR, et al. The PTPN2/PTPN1 inhibitor ABBV-CLS-484 unleashes potent anti-tumour immunity. *Nature* 2023;**622**: 850−62.
31. Raju GSR, Pavitra E, Bandaru SS, Varaprasad GL, Nagaraju GP, Malla RR, et al. HOTAIR: a potential metastatic, drug-resistant and prognostic regulator of breast cancer. *Mol Cancer* 2023;**22**:65.
32. Kornepati AVR, Vadlamudi RK, Curiel TJ. Programmed death ligand 1 signals in cancer cells. *Nat Rev Cancer* 2022;**22**:174−89.
33. Tang X, Chen Y, Wang B, Luo D, Wang J, He Y, et al. Autonomous feedback-driven engineered DNAzyme-coated trojan horse-like nanocapsules for on-demand CRISPR/Cas9 delivery. *ACS Nano* 2024;**18**:13950−65.
34. Li F, Song N, Dong Y, Li S, Li L, Liu Y, et al. A proton-activatable DNA-based nanosystem enables co-delivery of CRISPR/Cas9 and DNAzyme for combined gene therapy. *Angew Chem Int Ed Engl* 2022; **61**:e202116569.